Properties of projectile-fragments in the ^{40}Ar + ^{27}Al reaction at 44 A.MeV. Comparison with a multisequential decay model. [1]

M.Geraci, G. Lanzanò [2], E. De Filippo, A. Pagano

Istituto Naz. Fisica Nucleare and Dipartimento di Fisica
Via S. Sofia 64, I-95123 Catania, Italy

J.L. Charvet, R. Dayras, R. Legrain [3], C. Volant

DAPNIA/SPhN, CEA/Saclay, 91191 Gif-sur-Yvette Cedex, France

J. Richert, P. Wagner

CRN Strasbourg, BP 20 CR, 67037 Strasbourg Cedex, France

Abstract

Results on projectile fragment-fragment coincidences in the forward direction and for the reaction ^{40}Ar+^{27}Al at 44 A.MeV are presented and compared with the predictions of two different entrance channel models, a two-body and a three-body mechanism both followed by a binary multisequential decay including fission. This analysis shows that many features of the projectile decay products are well accounted for by the binary multisequential decay model. However the results depend critically upon the initial masses and excitation energies of the primary projectile fragments. In this respect, the three-body approach underestimates the excitation energy imparted to the primary fragments whereas the two-body scenario overestimates it. The present data put strong constraints on the initial excitation energy imparted to the primary fragments which appears to be intermediate between the predictions of the two models.

Key words: Intermediate energy, ^{40}Ar+^{27}Al reaction, E=44 A.MeV, projectile fragment, fragment-fragment coincidence, fragment velocity, excitation energy.

PACS: 25.70.Pq, 25.70.Mn

1 Introduction

In a previous paper [1] we have stressed the fact that, in general, the study of light particles and light fragments emitted in heavy ion nuclear reactions can give some insight on the involved reaction mechanisms. In that paper we have shown part of the results relative to the ^{40}Ar+^{27}Al reaction at 44 A.MeV concerning the emission of light particles in coincidence with projectile-like fragments (PLFs). The main conclusion of the paper was that the light-particle velocity spectra measured in an extended angular range from 1.5° to 172° can be well accounted for by assuming three emitting sources, one with a velocity close to the beam velocity, an other one with a velocity close to the target velocity, and a third one with a velocity intermediate between them. While the first two sources can be considered as thermalized, the third intermediate source which is located in the overlap zone of the two colliding nuclei is considered as the origin of "pre-equilibrium" or, more generally, "non-equilibrium" particles, having an "apparent" temperature around 15 MeV. The importance of this intermediate source is not negligible at all, its intensity being comparable to the two other ones. These findings have several consequences. On one hand the production of "hot" equilibrated nuclei in this intermediate energy regime is highly questionable, as a great amount of excitation energy is transferred to the intermediate source, allowing the production of light particles and intermediate mass fragments. On the other hand the vicinity in phase space of the intermediate source with respect to the two others, could alter the equilibrium properties of the projectile- and target-like fragment sources. These results led to the following reaction scenario [2]. The collision of the two nuclei is primarily the source of a highly perturbed zone of nuclear matter, from which particles and clusters of intermediate velocity escape. The parts of the projectile and of the target that are spatially less involved in this overlap zone, leave this zone with quite low excitation energy, bringing memory of the entrance reaction channel. They de-excite by emission of light particles and/or fragments with velocity close to those of the projectile and of the target respectively. Later, a coincidence experiment [3] between projectile-like and target-like (TLF) fragments using the same reaction (^{40}Ar+^{27}Al reaction at 44 A.MeV) showed a strong correlation between PLFs in the forward direction and TLFs detected in a wide angular range up to 90°. Both a three-body abrasion-ablation mechanism (low excitation energy in the primary PLFs and TLFs) or a simple two-body mechanism like the so-called "deep inelastic" collisions (high excitation energy in the primary projectile and target nuclei) were able to account rather well for the experimental results. This ambiguity,

---

Email address: `lanzano@ct.infn.it` (G. Lanzanò).
[1] Experiment performed at GANIL.
[2] Corresponding author.
[3] deceased

already noticed [4], finds its origin in the fact that different primary mass distributions associated to the proper excitation energy yield the same final mass product distributions. Thus the only way to distinguish between the different entrance channel models is through an experimental determination of the primary fragment mass and excitation energy distributions.

In this paper we want to add further information on the reaction mechanism involved in the ^{40}Ar+^{27}Al reaction at 44 A.MeV, studying the emission of the "fragments" accompanying PLFs in the forward direction. These primary "pieces" of nuclei can be highly excited, giving rise to further, more complex scenario of the fragmentation process. At these intermediate and higher energies, it has become widespread, although quite arbitrary, to divide the nuclear reaction products in light particles (Z<3), intermediate mass fragments (IMFs, 2<Z<x, where x is not well defined and depends on the studied system) and projectile-like or target-like fragments (PLFs or TLFs) with masses close to the projectile or the target mass respectively. This "nomenclature" often hides one or more reaction processes responsible (or supposed responsible) of the nuclear reaction products. In the present case, inclusive measurements [2] evidenced an excessive production of light ions centered at Z=6, with velocity close to the beam velocity (for simplicity we shall call in the following "light ions" the ions with charge 2<Z<10). While a simple abrasion-ablation mechanism could account for the properties of PLFs close to the mass of the projectile, it failed in the prediction of the abnormal abundance of PLFs with charge around Z=6.

In the following we shall try to give more insight on the excitation energy imparted to the primary projectile fragments and their de-excitation properties, studying all the emitted charged nuclear products essentially in the forward direction, where the projectile aspects are most prominent with respect to the other two sources. PLF-PLF coincidences will be considered and compared with the predictions of a multisequential decay mechanism [5,6]. We first describe shortly the experimental lay-out (section 2) and present the bulk of the experimental results in section 3, giving particular emphasis to projectile fragments with Z>2. In section 4 we describe the ingredients of the binary multisequential de-excitation model, applied to a two-body and a three-body reaction mechanisms. The comparison between theoretical predictions and the experimental results is made in section 5. Finally section 6 is devoted to the discussion and conclusions.

2   Experimental layout

The experiment has been performed at GANIL, by bombarding a 200 μg/cm^2 thick self-supporting ^{27}Al target with a 44 A.MeV ^{40}Ar pulsed beam. Details

on the experimental apparatus, the ARGOS multidetector, can be found in [1]. Shortly, the nuclear products were detected and charge identified from Z=1 up to Z=20 in a forward wall, centered at 0° around the beam and constituted by 60, 700 μm thick plastic - BaF$_2$ phoswiches read by photomultipliers. Their angular range extended from 1.5° ± 0.75° up to 6° ±0.75°. Each BaF$_2$ crystal had a hexagonal surface of 25 cm^2 and were 10 cm thick, stopping 200 MeV protons. Some additional phoswiches were positioned also in the horizontal plane from 10° to 150°. While the identification of light particles was possible in the entire angular range, the identification of Z≥3 particles was limited to the forward wall. Concerning the electronics, the signal from each photomultiplier was gated by the cyclotrons radio-frequency unit to get a timing signal which opened two gates. A narrow 30 ns wide gate and a 300 ns wide gate were used to integrate the photomultiplier signals to yield the fast and slow components respectively. The identification of charged nuclear products was achieved by making bidimensional contour-plots like those reported in Fig. 1 where the amplitude of the fast component is reported either as a function of the amplitude of the slow component (Fig. 1a) or as a function of the time of flight (Fig. 1b). For fragments with charge from Z=3 up to Z=20, charge identification within one unit is achieved in the fast-slow component bidimensional plot. An isotopic separation of Z=1 and Z=2 particles is obtained by using jointly the two plots. Due to the plastic thickness, an energy threshold is introduced in the fragment identification, increasing with the fragment charge, typically ≈15 A.MeV and ≈21 A.MeV for Oxygen and Sulfur ions respectively. However, this threshold hardly affects the fragment velocity spectra in the forward direction and for velocities close to the beam velocity. The locus of the ions stopping in the plastic is indicated by PL in Fig. 1a. The particle velocity was deduced from their time of flight.

3   Experimental results

As in the following we shall compare the predictions of a multisequential decay model with either inclusive or exclusive data from Ref.[1,2] and in particular with new data coming from the forward wall (present experiment), in this section we want to justify the choice of this model by giving an overview of the PLF properties, as seen in the forward wall.

3.1   Single data

Firstly we show in Fig. 2, the evolution with increasing angle (from 1.5° to 6°), of the PLF cross-section as a function of the fragment charge, from Z=1 to Z=20. We observe a rapid decrease (see also [2]) with the laboratory angle

4

of the production cross-section of those fragments with a charge close to the projectile one. This decrease is much smaller for the light ion region around Z=6, and is not present for light particles, Z<3. Ions with charge exceeding the charge of the projectile are also observed since reactions with exchange of a few nucleons between target and projectile are still important [8] at these high energies. For the light particle yield (Z≤2) and for Z=3 fragments, we have considered only the component with velocity close to the projectile velocity. In order to obtain this component, we have performed a three-source analysis of the velocity spectra as a function of the laboratory angle, as in Ref.[1], but disregarding the coincident fragment on the wall. For Z=3 particles this analysis is less accurate, because of the limited angular range examined and the fact that the fragments are not resolved in mass. For Z≥4 PLFs the whole velocity spectrum (see below and Fig. 4) has been integrated in order to get the cross-sections reported in Fig. 2. The angle integrated PLF production cross-section is reported in Fig. 3 as a function of the PLF charge. Given our limited PLF angular distribution on the wall, from 1.5° to 6°, for larger angle, we have taken into account the absolute inclusive values measured for the same reaction in Ref. [2]. As the angular distributions are steeper for PLFs with charge close to the projectile charge and flatter for light ions, these corrections become more important as the PLF charge decreases. Note the overproduction of light ions around Z=6, probably due to a binary break-up of excited primary projectile-fragments.

Fig. 4 shows the velocity spectra for some selected ions from Z=5 up to Z=17 detected in the forward wall, at 3°. While the maximum of these spectra corresponds always to a velocity very close to the beam velocity (8.9 cm/ns), their width, starting from Z=18, is increasing as the fragment charge decreases. Furthermore they present a characteristic tail towards low energy [2]. Highly dissipative deep inelastic transfer reactions have been invoked to explain the particular shape of these velocity spectra [9]. To fix in a quantitative way the features of these spectra, we have fitted the high velocity side with gaussian functions starting at a low velocity corresponding to ≈80-90% of the maximum yield. For fragments detected at 3°, the velocity corresponding to the maximum of the gaussian fit and its width (standard deviation) are reported in Fig. 5, respectively as full points and bars, as a function of the fragment charge. A typical S-shaped behaviour of the ion velocity as a function of the ion charge is observed. This velocity reaches a maximum value at the Z of the projectile. Fragments with Z>18, result from the pick-up of few nucleons from the target, leading to a slowing down of the projectile [8]. For Z<18, a minimum is reached in the region of light ions, around Z=7, and then the velocity increases again for lighter ions. We note, however, that this velocity is always very close to the beam velocity, between 8.3 and 8.7 cm/ns (this has been checked for all the detectors in the wall). The variance of the gaussian fits to the high velocity side of the velocity spectra, increases monotonously as one moves away from the projectile.

The experimental fragment-fragment charge correlation is displayed in the bidimensional plot of Fig. 6, starting from Z=3. For reason of clarity Z=1 and Z=2 particles have not been included in the plot. They constitute the most important part of the projectile fragments, and their study as a function of the coincident heavy fragment in the wall has been carried out previously [1]. Light particle correlation studies can also give insight on the emission time sequence [10]. Two features stand out from Fig. 6: a maximum in the zone of light fragments, centered around $Z_1=Z_2=6$ and a population of events close and along the line $Z_1 + Z_2=18$. This experimental observation gives first evidence for the presence in this reaction of break-up or fission processes of the projectile and/or primary projectile fragments, and accounts for the excess of light ions observed in [2] and in the present experiment. Furthermore, there is evidence that light ions can be produced in well-defined unbound excited states, allowing for subsequent break-up and production of lighter ion and/or light particles. As an example, we show here that the most abundant light ion observed in this reaction, i.e. carbon, is also produced in some unbound excited states, well known from low-energy nuclear reactions.

We start from the experimental evidence that a huge quantity of α-particles ($\approx$10% of the α-particles detected on the wall) are well correlated to form ^{8}Be, either in its ground or excited states. Without going into details (see [10] and references therein), the experimental correlation function is constructed by dividing the coincidence yield by the yield of uncorrelated events. Fig. 7a shows this correlation function for 2 α-particles detected in the wall, as a function of their relative momentum. The peaks corresponding to the ground state and to the broad first excited level of the ^{8}Be at 3.04 MeV are indicated. The peak at $\approx$45 MeV/c is generally attributed to the neutron unstable level of ^{9}Be at 2.43 MeV. We have reconstructed the spatial and kinematic properties of the primary ^{8}Be ions in its ground-state and then looked for further coincidences between this primary ^{8}Be and α-particles or protons. The correlation function (not divided by the uncorrelated yield) for ^{8}Be and α-particles is shown in Fig. 7b. The well known excited states in ^{12}C at 7.65 and 9.64 MeV [11] and other not resolved states at even higher excitation energies are evidenced in Fig. 7b. In a similar way the correlation function between protons and the reconstructed ^{8}Be (not shown), leads to the strong peak relative to the ^{9}B ground state. Correlations between Li and α-particles show strong evidence for the population of the (9.19+9.27 MeV) and the (9.88+10.26+..MeV) excited states [11] in ^{11}B [12].

To summarize these results, the small cone around 0° and covered by our wall is mainly populated by particles and fragments with a velocity very close to the beam velocity. Fragment-fragment coincidence suggests that light ions may

have their origin in primary excited fragments that decay by a fission (break-up) process. These light ions are produced either in their ground state or in bound and unbound excited states, these latter can be the source of a huge quantity of well-correlated light particles. For some of them, especially light fragments like ^{11}B and ^{12}C, it is also possible to trace back their emitting levels, starting from the detected coincident particles. However, this is generally not possible, because our apparatus is not sensitive to the fragment mass.

These experimental findings led us to consider a multisequential mechanism, as responsible for the production of the projectile (and target) fragments. The next section will be devoted to the description of two extreme entrance channel models, respectively a two-body and a three-body model, both incorporating the same binary multisequential decay mechanism.

4 Description of the models

Starting from the coincidences between projectile fragments and light particles it was found previously (see Fig. 12a) in [1]) that the reconstructed primary PLF charge was close to the projectile charge, showing however a decreasing behaviour as the experimental PLF charge decreased. In other words, the reconstructed primary PLF charge was lying in-between the charge of the projectile (as expected if a pure two-body mechanism was involved) and the charge of a primary PLF obtained with a three-body process, leading to the formation of a fire-ball and a PLF and TLF remnants, in consequence of a geometric abrasion mechanism [2]. After the presentation of the binary multi-sequential model, we attempt to describe the properties of the decay products of the projectile and target primary fragments under these two extreme assumptions leaving aside any preequilibrium emission.

4.1 Multisequential decay model

In the subsequent calculations, we assume that the primary excited fragments are fully equilibrated and can then de-excite by particle or cluster emission or by fissioning, in a chain process, until the available excitation energy is exhausted. The formalism of this multisequential de-excitation process is de-scribed extensively in Ref. [5,6].

Briefly, for a given temperature the excited nucleus disassembles in its refer-ence frame. It follows a chain of binary decays, generating at each step two new fragments which themselves may decay in two further fragments [5]. The process is numerically simulated by following the decaying system in space

7

under the constraint that the total energy of the system is conserved at each step [6]. The decay stops when the excitation energy is lower than the smallest emission threshold.

The essential ingredients which govern the disassembly are the binary decay rates which fix at each step the probability with which a given two-body decay can occur. These rates are either those which are given by the Weisskopf theory [13] or those given by the approach of Swiatecki [14]. In the first case the rates are essentially determined as the ratio of the energy level densities of the initial and final fragments. In the second case the disassembly is described as a fission-like process.

Both types of calculations have been performed. Slightly better results were obtained with the Swiatecki approach and only the corresponding results will be shown in the following.

4.2   The binary reaction hypothesis

For the same reaction, it has been shown previously [3] that PLF-TLF coincidence data could be interpreted as the result of a two-step process: a binary collision between the projectile and the target with a very small net exchange of nucleons leading to primary excited projectile and target nuclei which then decay by particle emission. Within this hypothesis, it was shown that the projectile and target primary fragments share an amount of excitation energy which evolves from equal sharing for peripheral collisions to sharing in the mass ratio (equal temperature) for more central collisions. However as the mass asymmetry is weak, this evolution was not very strong. For the sake of simplicity we will assume here that the masses and atomic numbers of the primary PLFs and TLFs are strictly those of the projectile and of the target and that the excitation energies are shared in the ratio of their mass (equal temperature hypothesis). The primary PLFs and TLFs are assumed in thermal equilibrium at a temperature T, yielding excitation energies $E_P^* = (A_P/8)T^2$ and $E_T^* = (A_T/8)T^2$ for the primary PLFs and TLFs respectively. Here A_P (E_P^*) and A_T (E_T^*) are the mass (excitation energy) of the projectile and of the target respectively. We have taken $A/8$ for the level density parameter. For the sake of simplicity, we have supposed that all temperatures are equiprobable from $T_{min} = 0.5$ MeV up to a value T_{max} which is left as a free parameter to be determined by a comparison with the experimental data. The minimum value of the temperature $T_{min} = 0.5$ MeV which corresponds to excitation energies of 0.84 MeV and 1.25 MeV in the target and the projectile respectively has been chosen in order to reject elastic scattering events. Furthermore, we have assumed that the primary PLF deflection angle increases with temperature (the more violent is the collision, the larger is the deflection angle and

8

the larger is the temperature). For a given temperature T, the projectile angular distribution is taken as $Y(\theta) \propto \exp(-\theta^2/2\sigma^2)$, with $\sigma = aT^2$ and a a free parameter to be adjusted by a comparison with the experimental data. Then, for a given temperature which fixes the excitation energy of the system and some diffusion angle of the projectile, a usual two-body kinematics is used to determine the velocity of the excited projectile and the emission angle and the velocity of the excited target.

The value of T_{max} is obtained by comparing the results of the calculation to the angle-integrated projectile fragment production cross-section of Fig. 3. Indeed, for low-values of $T_{max} \approx$ 3-4 MeV, the calculation, as expected, gives a U-shape distribution, with a low branch corresponding to light particles whereas the high branch is associated to projectile fragments with charge very close to the projectile charge, with a pronounced minimum near Z=9 fragments. On the contrary, for $T_{max} \approx$ 9-10 MeV the yield of light particles and light fragments is overpredicted with respect to the yield of PLFs with charge close to the projectile charge. The best agreement between experimental and calculated distributions is obtained for T_{max} = 7.1 MeV, as shown by the full line in Fig. 3. This value is somewhat lower than the limiting value $T_{lim} \approx 9$ MeV which is the energy available in the CM system. The use of a more realistic temperature distribution, like for instance a triangular distribution (obtained by weighting with the impact parameter) does not significantly improve the agreement between the calculations and the experimental data.

Once the value of T_{max}= 7.1 MeV has been fixed, we have adopted a similar method to determine the parameter a of the primary PLF angular distributions. This parameter has been varied from 0.016 to 0.34 MeV^{-2}. Low values of a tend to overpredict the PLF production at the most forward angles of 1.5°, and to underpredict their production at 6°. For each value of a, the results of the calculation have been compared simultaneously to the PLF distributions at all angles from 1.5°, to 6°. The best agreement has been obtained for a=0.254 MeV^{-2}, as shown by the full lines in Fig. 2.

Once T_{max} and a are fixed, the calculations proceed as it follows. For each event, a value of the temperature T is chosen at random between 0.5 MeV and T_{max}. The azimuthal angle ϕ of the projectile is taken at random between 0° and 360° whereas its deflection angle θ is drawn from the distribution $Y(\theta)$. For each event the whole de-excitation process is followed for both the excited projectile and target nuclei. Finally the total number of events has been normalized to the total reaction cross-section estimated to be σ_R=2.4 barns according to Ref. [15].

To summarize, the present two-body approach relies on two strong hypotheses: i)the projectile and the target are excited in binary encounters with no net mass exchange. ii)all the dissipated energy is converted into excitation of the

projectile and of the target according to their mass (thermal equilibrium). It is clear that a full description of the experimental data is out of the scope of the model. Indeed about 1/3 of the light particles emitted out of equilibrium [1] are not taken into account. However, a detailed comparison with the data may give information to what extent the above hypothesis are violated.

4.3   Three-body model

In this model, see Ref. [2], three bodies are supposed emerging from the reaction after an abrasion mechanism. Most of the excitation energy is concentrated in the so-called "fire-ball" (FB), that is formed in the geometric overlap zone between the projectile and the target. Hence, less excitation energy than in the previous model is deposited in the projectile and target primary fragments. The primary projectile fragments are assumed to have gaussian angular distributions, centered at 0°, of the form $Y(\theta) \propto \exp(-\theta^2/2\sigma^2)$, with σ parameterized, following Goldhaber [16], as: $\sigma = \sigma_0 \sqrt{(A_{PF}(A_P - A_{PF})/(A_P - 1))}$. Here A_{PF} stands for the primary PLF mass. The parameter σ_0 has been adjusted to reproduce the experimental projectile fragment angular distributions, $\sigma_0 = 2.6°$. The deflection angle for the target fragment is obtained by imposing energy and momentum conservation to the three bodies (PLF, TLF and FB) [2]. For each impact parameter, the three primary fragment masses, velocities and excitation energies are obtained by the program ABRADE in its pure geometrical version. Indeed, in Ref. [2] the geometrical abrasion model has been modified, by adjusting the separation energies, in order to better reproduce the correlation between the measured fragment masses and their velocities. This reduction of the separation energies results in a decrease of the already low excitation energies imparted to the spectators. These considerations led us to stick to the purely geometrical version of the model. The projectile and target fragment charges are obtained by supposing that the initial projectile and target proton to neutron ratios are kept by the respective primary fragments. As for the two-body mechanism, the multisequential model is then applied to the primary fragments, until they cannot anymore de-excite. Here also the total reaction cross-section is used for absolute normalization.

In contrast with the two-body approach here, the primary PLF's and TLF's masses decrease strongly with the impact parameter whereas their excitation energies (which increase as the impact parameter decreases) are small. Thus they emit few light particles and almost no fragments. Most of the energy is dissipated in the overlap zone which is an abundant source of high energy light particles and fragments.

5 Results

Before comparing the predictions of the models with the experimental results, some general features of the two-body binary multisequential decay model are presented.

5.1 General results of the binary multisequential decay calculations

In this sub-section some general predictions of the multisequential decay model are presented that cannot be compared directly with our experimental data, concerning, for instance, the "event structure", the event multiplicity and its relation with the initial temperature.

Fig. 8a shows the multiplicity distributions M_{tot} and M_{cp} respectively including (dashed line histogram) or excluding (full line histogram) neutrons. For the M_{tot} distribution, the M=1 events correspond to very peripheral collisions in which the ^{40}Ar projectile remains in its ground state or is excited below its particle emission threshold and thus decays only by γ-ray emission. The M=2 channel is dominated by one neutron emission. The M_{tot} distribution extends up to M=18, whereas the M_{cp} distribution reaches only M=12, showing the importance of neutron emission.

When M_{tot} becomes equal or greater than 9, a certain number of events are composed only of light charge particles Z≤2 and neutrons and are of the same nature as the vaporization events seen in the reaction $^{36}Ar+^{58}Ni$ and reported in Ref. [17]. The cross section for these events reaches 4.7 mb representing roughly 2.10^{-3} of the reaction cross-section. This value is much higher than the one found in [17]. But it has to be noted that in this last case, the cross sections were given for the vaporization of the whole system (projectile+target). According to the calculation vaporization occurs when the initial temperature exceeds 6.7 MeV.

Fig. 8b shows the evolution of the average temperature $< T >$ of the projectile as a function of the total multiplicity M_{tot} (full circles) and of the total charged particle multiplicity M_{cp} (open circles). At low multiplicities (M_{tot} or M_{cp}), the average temperature $< T >$ increases almost linearly with the multiplicity up to $< T >\simeq 6$ MeV at which point $< T >$ starts to saturate to reach the limiting value of $\simeq 7$ MeV close to T_{max}. For a given average temperature in the projectile, the offset between the M_{tot} curve and the M_{cp} curve is just the number of emitted neutrons. This number increases progressively with temperature from $\simeq 1$ at $< T > = 1$ MeV to $\simeq 6$ for $< T > = 6$ MeV.

5.2 Comparison between experimental and theoretical results

In this section the predictions of the binary multisequential decay model assuming either a 2-body or a 3-body primary process are compared to the experimental data.

The predicted PLF charge distributions as a function of the detection angle from 1.5° to 6.0° are compared to the experimental data in Fig. 2, whereas the angle integrated charge distributions are presented in Fig. 3. The full lines are obtained in the framework of the 2-body hypothesis whereas the dashed lines are obtained assuming a 3-body process. The two hypotheses yield a reasonable agreement with the data except for light particles (n, Z=1 and Z=2) and to a less extent for the integrated yields of light fragments around Z=6 for which the 3-body process underpredicts the production yield. In the three-body description, the low excitation energies of the primary fragments are compensated in part by the decrease of the primary masses as the impact parameter decreases. Although the final charge distributions are well reproduced down to $Z \simeq 10$, the yields of light particles and fragments are underpredicted signaling insufficient excitation energies in the primary fragments. Whatever the primary process, the multisequential decay model predicts the emission of a large quantity of neutrons. For instance, the number of neutrons emitted at 1.5°, overcomes by almost a factor of ten the number of particles with Z=1 or Z=2 emitted at the same angle. This overwhelming neutron emission, has been observed experimentally [1]. Probably it is due to the particular nature of the projectile, a neutron-rich nucleus.

The PLF velocity spectra (hatched histograms) calculated at a laboratory angle $\theta_{Lab}=3°$, from Z=17 down to Z=5, are compared to the experimental ones in Fig. 4 assuming either a 2-body (left panel) process or a three-body (right panel) mechanism. At this very forward angle, when the PLF charge is less than 14 both models predict in addition the production of a low velocity TLF fragment. The high velocity part of the spectra, see also Fig. 5, is well reproduced by the two-body model. As far as the three-body calculation is concerned, the overdamping observed when the Z of the PLF's decreases is expected and was noticed previously [2] when using the abrasion model in its purely geometrical form. In order to alleviate this effect, separation energies were allowed to evolve from the liquid drop limit to the abrasion limit in Ref. [2]. One notes also that the calculated spectra are narrower than in the two-body case. This again reflects the lower excitation energy imparted to the primary PLF's in the three body scenario. The low velocity tail observed in the experimental spectra is not reproduced by either model.

Fig. 9 shows the single proton (left panel) and α-particle (right panel) velocity spectra at different laboratory angles, ranging from 1.5° to 172°. The present

data (full circles) were obtained by subtracting the intermediate velocity component from the experimental velocity spectra. The calculated spectra within the two-body scenario taking into account particle emission from the excited projectile and target are indicated by the full line histograms. These spectra are in very good agreement with the experimental ones, in shape as well as in magnitude. For consistency, in the case of the three-body calculations only emissions from the PLFs and TLFs were taken into account. The calculated proton and alpha velocity spectra are shown by the hatched histograms in Fig. 9. Although the general shape of the spectra is well reproduced, the component resulting from PLF emission is too low in energy. This again is due to the overdamping of the PLF's as predicted by the abrasion model. The low yields as compared to the experimental data is a manifestation of the too low excitation energy imparted to the primary fragments.

Fig. 10a compares the calculated isotopic distributions of Z = 8, 13 and 16 PLFs calculated within the two-body scenario (histograms) to the measured ones at 2.5°. Fig. 10b shows the experimental (full circles) and calculated (open circles) average $< A/Z >$ ratios as a function of the Z of the PLFs at the same detection angle. There again, the calculation is in good agreement with the data. We note that the measured $< A/Z >$ ratio is about 0.1 unit lower than the A/Z=2.22 of the projectile. This ratio depends slightly upon the emission angle and the Z of the PLF. The strong dependence of the PLF isotopic distributions from the projectile A/Z ratio, a sort of "memory effect", has been evidenced in [18]. The standard deviation of the isotopic distributions indicated by the vertical bars in Fig. 10b increases as the PLF charge decreases.This tendency is well reproduced by the calculation. Finally Fig. 10c shows the absolute isotopic distributions for Z=1 and Z=2 particles emitted by the PLFs, integrated over velocity and angle. The agreement between the experimental distributions (full and empty circles) and the calculation (full line and dashed line histograms) is quite satisfactory. That the absolute cross sections are well reproduced is not surprising as the absolute angular charge distributions (Fig. 2) and the absolute fragment charge distributions (Fig. 3) have been used to tune the parameters (T_{max}, a) of the model. More interesting is the fact that the isotopic distributions are well rendered by the binary multisequential model. Note that the production of ^{5}He considered stable in the model will not change the present agreement. In particular, both experiment and model show evidence for an equal amount production of protons and α-particles, for this system and at this incident energy.

In Fig. 11 are presented the fragment charge correlations as calculated with the two-body entrance channel model (Fig. 11a) and the three-body approach (Fig. 11b). They can be compared to the experimental charge correlation presented in Fig. 6. The excess of population observed near $Z_1 \simeq Z_2 \simeq 6$ is well reproduced by the two-body calculation whereas it is missed by the three-body one. On the other hand, the peaks near $Z_1 \simeq Z_2 \simeq 3$ and $Z_1 \simeq 3, 7$

13

and $Z_2 \simeq 7, 3$ are better taken into account by the three-body approach. One of the marked differences between the data and the two calculations lies in the population near the $Z_1 + Z_2 = 18$ line. Relative to the data, this region is overpopulated in the two-body calculation whereas it is completely depleted in the three-body one. The origin of this difference can be found in the assumed mass of the primary PLF's, the projectile in the first case, the projectile spectator after the abrasion process in the second case.

Fig. 12 gives more quantitatively the production cross-section of some projectile fragments, ranging from Li up to P, as a function of the coincident fragment charge assuming a two-body entrance channel. Both the behaviour and the absolute values are well reproduced. The measured large fragment-fragment coincidence yields cannot be reproduced by a standard evaporation code. In this respect the use of the binary multisequential decay model constitutes a real success. One notes, in Figs. 6 and 12, the presence of events for which $Z_1 + Z_2 \geq 18$. These events probably result from the transfer of few nucleons from the target to the projectile followed by a fission or break-up process. Neither models, in their present formulations, can account for this class of events.

Finally, Fig. 13 shows as a function of the final fragment charge, the excitation energy per nucleon of the primary projectile as given by the two-body model (upper dashed curve) and the primary projectile fragment excitation energy per nucleon as given by the three-body model (lower dashed curve). The experimental values (full circles) have been obtained by a calorimetric method making use of the measured light particle velocity spectra [1]. The experimental data lie in between the predictions of the two models. The two-body scenario overpredicts the excitation energies while the reverse is true for the three-body approach. The discrepancy between the experimental values and those given by the two-body model is surprising as the parameters of the model were adjusted in order to fit the experimental yields and angular distributions (Figs. 2-3). In order to understand this disagreement, it was decided to apply to the simulated events, the calorimetric method used in ref. [1] to determine the excitation energy of the primary PLF's. For a given event, in the projectile frame of reference, this excitation energy is defined as,

$$E_{PLF}^* = M_{PLF}c^2 + \Sigma_i(m_ic^2 + K_i) - M_{PLF}^*c^2$$

where M_{PLF} is the mass of the final PLF, m_i and K_i are respectively the mass and the kinetic energy of particle i and M_{PLF}^* is the mass of the primary projectile fragment taken as the sum of the masses of the residual PLF and of the emitted light particles. The sum runs over all light particles (neutrons to Z=2 isotopes) emitted by the projectile. As it was done for the experimental data, the kinetic energy of the final PLF as well as the contributions from fragments with $Z > 2$ are neglected. Taking into account all reaction products

but still neglecting the kinetic energy of the final PLF increases the deduced excitation energy per nucleon by no more than 200 keV. The excitation energies per nucleon thus computed are presented as full squares in Fig. 13 and are in much better agreement with the experimental values. This lowering of the excitation energy using the calorimetric method is due to a small part to the neglect of the residual excitation energy of the final PLFs produced below particle emission threshold. The main effect comes from neglecting the kinetic energy of the final PLFs. The lighter is the final PLF, the larger is the effect. This means that the excitation imparted to the primary projectile fragments as determined in ref. [1] are certainly underestimated. The remaining discrepancy between the data and the two-body prediction can be ascribed to a large part to the mass of the primary fragments which are the projectile and the target in the two-body model. This is certainly not true as we know from a previous experiment [1] that approximately one third of the light particles are produced at mid-rapidity in the overlap zone between the projectile and the target. Thus, the masses of the primary fragments are expected to decrease as the impact parameter decreases. On the opposite, the masses of the spectators predicted by the geometric abrasion model are too small, in other words only a fraction of the participant zone contribute to the mid-rapidity source, the rest of the nucleons remaining attached to the spectators, contributing to their excitation energies. Recently, a more realistic approach has been taken by Lacroix et al. in the HIPSE code [21]. Based on the sudden approximation, the approaching phase of the collision, leading to the maximum overlap between the projectile and the target is governed by a parameter (α_a) which defines the interaction potential at distances smaller than the distance of contact. As in the three-body scenario, the quasi-projectile and the quasi-target are initially defined as those nucleons not belonging to the overlap zone. At this point, a fraction (x_{tr}) of the nucleons in the overlap, initially belonging to the projectile (or the target) are transferred to the target (or projectile). This nucleon transfer increases the mass of the quasi-projectile and of the quasi-target and contributes to their excitation energy. Another fraction (x_{coll}) of the nucleons in the overlap undergo nucleon-nucleon collisions at the origin of fast particle emission. The model thus depends upon three parameters $(\alpha_a, x_{tr}$ and $x_{coll})$ which are adjusted on experimental data. For quasi-symmetric systems, these parameters depend essentially upon the bombarding energy.

6 Discussion and conclusions

Despite its simplicity, the multisequential decay mechanism describes many features of projectile fragments produced in heavy ions collisions at intermediate energy. It is particularly efficient in describing the decay of the excited primary fragments reproducing adequately the competition between light par-

15

ticle emission and fragment production. Indeed, it is not possible using standard evaporation codes to reproduce the large yields of fragment-fragment coincidences observed experimentally.

We observe that this agreement is not restricted only to the present reaction study. As shown in [19] many aspects of the reaction induced by 8.1 GeV protons on gold, and in particular the fragmentation process, are well reproduced by the present multisequential binary mechanism.

As a possible criticism to the present model, we observe that it relies on the assumption that the sequential decays are independent of each other and correspond to a system which stays in thermodynamical equilibrium all along its decay. This point may be questionable. Indeed the Weisskopf formulation leads to decay rates which for large excitation energies correspond to very short decay times. The Swiatecki formulation leads to somewhat longer times, but these may be quite short too. In both cases and for high excitation energies however these binary decay times are shorter than the characteristic times over which the Coulomb emission barrier changes for the following emission [20]. Even though the process certainly proceeds as succession of break-ups, the degree of realism of the present description is not clearly established when the excitation energy gets large.

Finally, note that a simplifying scenario has been introduced before applying this multisequential binary decay. At these bombarding energies, a reaction mechanism more reminiscent of " deep inelastic" collisions is favoured against the "fire-ball" hypothesis which works better at relativistic energies.

A full description of the experimental data is hampered by the lack of a reliable entrance channel model. Here, we have used two very schematic models in order to study how the mass distributions of the primary fragments and their excitation energy affect the properties of the final reaction products.

In the two-body approach, neglecting preequilibrium emission, it is assumed that the projectile and the target preserve their identity through the collision and are excited in proportion to their mass (thermal equilibrium hypothesis). The excitation energy imparted to the projectile and to the target is governed by the parameter T_{max} without any explicit dependance upon the impact parameter. This dependance is implicitly taken into account through the parameter a which determines the deflection angle of the projectile as a function of the violence of the collision (or the initial temperature). Although many features of projectile fragmentation at intermediate energy are well reproduced within this framework, some shortcomings of this approach are already revealed in Fig. 13. The excitation energy imparted to the primary PLF's (the projectile in this case) is slightly too high as compared to the data. To cure this deficiency, it would be necessary to include explicitly a

dependance of the primary PLF's mass and excitation energy on the impact parameter. Indeed, the same final products can be reached starting from less excited lower mass primary PLF's. This, at the same time would allow room for preequilibrium emission.

Concerning the three-body approach, it includes in a natural way a dependance of the primary PLF's mass and excitation energy upon the impact parameter. Only one parameter is used to govern the degree of energy damping. However, the separation of the system into two spectators (the projectile and the target remnants) and a participant zone given by the geometrical overlap of the projectile and the target at a given impact parameter, which may be valid at relativistic energy is not accurate at intermediate energy. This is apparent in Fig. 13 where the excitation energies of the primary PLF's computed within this approach are too low. This is the opposite effect seen with the two-body calculations. The mass and the excitation energy of the PLF's are too low.

Acknowledgements

References

[1] G. Lanzanò, E. De Filippo, M. Geraci, A. Pagano, S. Aiello, A. Cunsolo, R. Fonte, A. Foti, M. L. Sperduto, C. Volant, J. L. Charvet, R. Dayras, R. Legrain, *Nucl. Phys.* **A683** (2001) 566.

[2] R. Dayras, A. Pagano, J. Barrette, B. Berthier, D. M. de Castro Rizzo, E. Chavez, O. Cisse, R. Legrain, M.C. Mermaz, E. C. Pollacco, H. Delagrange, W. Mittig, B. Heusch, R. Coniglione, G. Lanzanò, A. Palmeri, *Nucl. Phys.* **A460**, (1986) 299.

[3] R. Dayras, R. Coniglione, J. Barrette, B. Berthier, D. M. de Castro Rizzo, O. Cisse, F. Gadi, R. Legrain, M. C. Mermaz, H. Delagrange, W. Mittig, B. Heusch, G. Lanzanò, A. Pagano, *Phys. Rev. Lett.* **62** (1989) 1017.

[4] D. J. Morrissey, L. F. Oliveira, J. O. Rassmussen, G. T. Seaborg, Y. Yariv and Z. Fraenkel, *Phys. Rev. Lett.* **43** (1979) 1139.

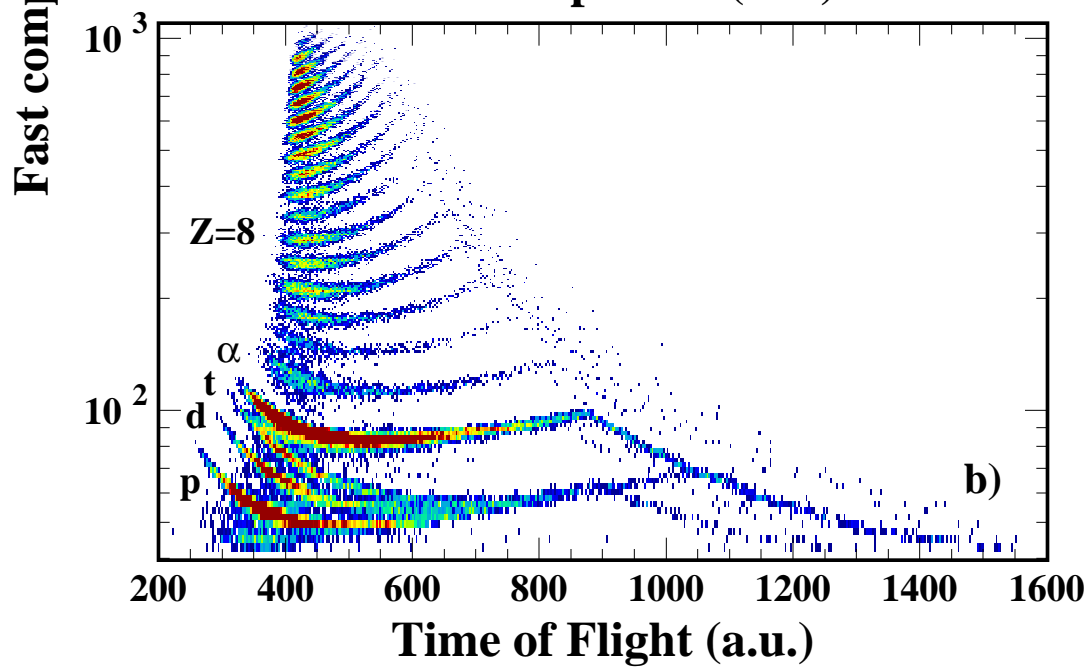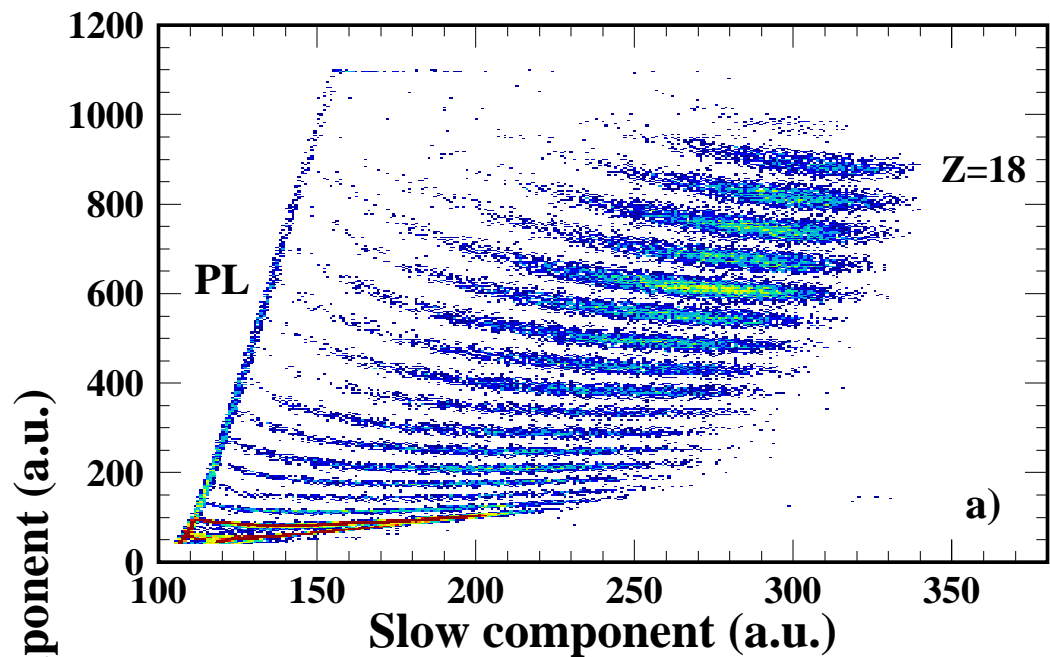[5] C. Bargagallo, J. Richert and P. Wagner, *Z. Phys.* **A324** (1986) 97.

[6] J. Richert and P. Wagner, *Nucl. Phys.* **A517** (1990) 399.

[7] G. Lanzanò, A. Pagano, E. De Filippo, S. Urso, C. Volant, B. Berthier, J. L. Charvet, R. Dayras, R. Legrain, R. Lucas, C. Mazur, E. Pollacco, J. E. Sauvestre, C. Beck and B. Djerroud, *Nucl. Instr. Meth. in Phys. Res.* **A332** (1993) 161.

[8] M. C. Mermaz, R. A. Dayras, J. Barrette, B. Berthier, D. M. de Castro Rizzo, O. Cisse, R. Legrain, A. Pagano, E. Pollacco, H. Delagrange, W. Mittig, B. Heusch, G. Lanzanò, A. Palmeri, *Nucl. Phys.* **A441** (1985) 129.

[9] L. Tassan-Got and C. Stéphan, *Nucl. Phys.* **A524**, (1991) 121.

[10] R. Ghetti et al., *Phys. Rev.* **C70** (2004) 027601; R. Ghetti et al. *Nucl. Phys.* **A765**, (2006) 307

[11] F. Ajzenberg-Selove, *Nucl. Phys.* **A506** (1990) 8 and 58.

[12] M. Geraci, Doctoral Thesis (unpublished), Università di Catania, 1997.

[13] V. F. Weisskopf, *Phys. Rev.* **52** (1937) 295.

[14] W. J. Swiatecki, *Aust. J. Phys.* **36** (1983) 641.

[15] R. J. Karol, *Phys. Rev.* **C11** (1975) 1203.

[16] A. S. Goldhaber, *Phys. Lett.* **53B** (1974) 306.

[17] Ch. Bacri et al., *Phys. Lett.* **B353** (1995) 27.

[18] G. Lanzanò, E. De Filippo, A. Pagano, E. Berthoumieux, R. Dayras, R. Legrain, E. C. Pollacco, C. Volant, *Phys. Lett.* **B332** (1994) 31.

[19] P. Wagner, J. Richert, V. A. Karnaukhov, H. Oeschler, *Phys. Lett.* **B460** (1999) 31.

[20] J. Richert and P. Wagner, *Phys. Rep.* **350** (2001) 1.

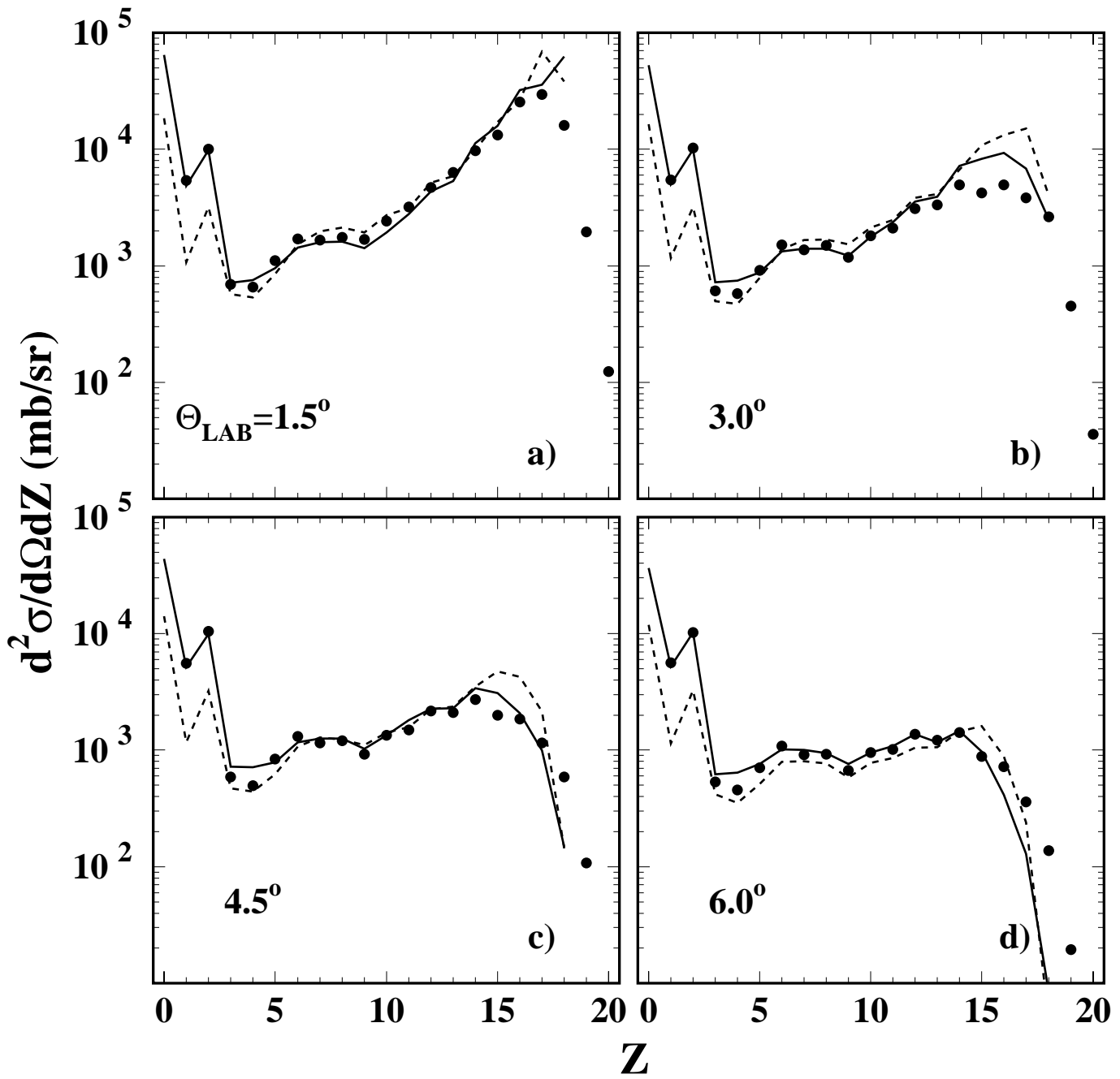[21] D. Lacroix, A. Van Lauwe and D. Durand, *Phys. Rev.* **C69** (2004) 054604.
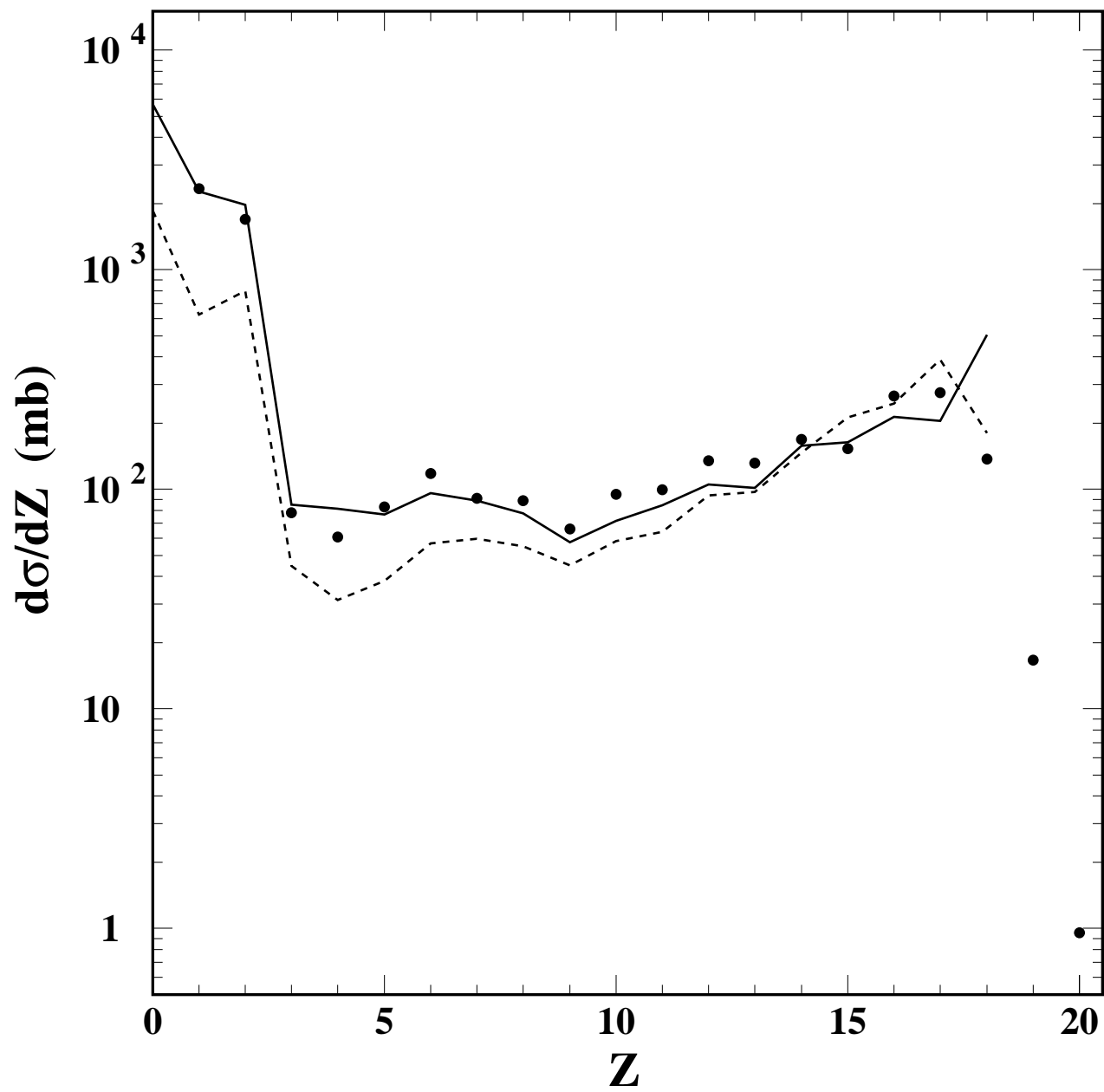
Figure Caption

Fig. 1 a) The fast light component is plotted as a function of the slow light component, and b) as a function of the time-of-flight for projectile fragments detected at 3° in the forward wall. Note the PLF charge resolution in (a), from Z=1 to Z=19. Isotopic resolution is also achieved for Z=1 particles (b). The lines for Z=18 (a), p, d, t and Z=8 (b) are indicated as references. The line indicated as PL in (a) is due to charged particles stopping in the 700 μm thick plastic. Nuclear reactions induced in the crystal by neutron and light charged particles [7] can be identified close and below the proton line in (b). Finally, note that in (b) particles with beam velocity are located at channel ≈420).

Fig. 2 Evolution of the projectile fragment charge distributions with the laboratory detection angle. The full and dashed lines are the results of calculations based, respectively, on two- and three-body models, including a multisequential binary-decay mechanism. See text for details.

Fig. 3 Angle-integrated projectile fragment charge distribution (full circles). The full and dashed lines are the results of calculations based, respectively, on two- and three-body models, including a multisequential binary-decay mechanism. See text for details.

Fig. 4 Laboratory velocity spectra at 3° for some projectile fragments (B, O, Na, Si, Cl). The experimental spectra are shown as full line histograms. The ion detection thresholds are indicated by arrows on the left side of the figure. The predictions of two- and three-body models including a multisequential binary-decay mechanism are shown respectively as hatched (left panel) and doubly-hatched (right panel) histograms. The projectile velocity is 8.9 cm/ns. Note that calculations include also the production of target fragments (TLF).

Fig. 5 Most probable value and standard deviation for gaussian functions fitting the high velocity part of the PLFs velocity spectra (see text and also Fig. 4) measured at 3° as a function of the PLFs atomic number (full circles and vertical bars respectively). In a similar way, the predicted most probable velocities of two- and three-body models including a multisequential binary-decay mechanism, are shown as thick full and thick dashed lines respectively. The predicted widths of the high velocity part of the spectra are also reported as lower and upper limits (thin full and thin dashed lines respectively) with respect to the most probable velocity lines (shadowed area). The position of the beam velocity is indicated by the dotted line.

Fig. 6 Bidimensional plot showing the experimental fragment-fragment charge correlation in the forward wall. As a reference, the line $Z_1 + Z_2$=18 is shown. The contour plot is linear according to the scale given on the right.

Fig. 7 a) $\alpha - \alpha$ correlation function in the forward wall, as a function of their relative momentum. The insert shows, the ^8Be 3.04 MeV excited level and, at lower relative momenta, a peak attributed to the ^9Be 2.43 MeV

excited level. b) Relative momentum distribution in the forward wall between an α-particle and a reconstructed ^8Be nucleus in its ground state. The two main excited levels in the primary ^{12}C nucleus are shown.

Fig. 8 a) The calculated total (including neutrons) M_{tot} and charged product M_{cp} multiplicity distributions are indicated by the dashed line histogram and the full line histogram respectively. b) The average initial temperature of the projectile is reported either as a function of the total multiplicity (full circles) or as a function of the charged product multiplicity (open circles). The bars accompanying each symbol give the standard deviation from the mean temperature.

Fig. 9 Velocity spectra for protons (left panel) and for α-particles (right panel) at different detection angles from 1.5° to 172°. The experimental spectra are shown by the full circles. Note that the mid-rapidity source-component has been subtracted from the experimental spectra(see text and ref. [1]). The predictions of the two-body calculations are shown by the full line histograms whereas the results of the three-body model are shown by the hatched histograms (see text for details).

Fig. 10 a) Isotopic distributions of projectile fragments with charge Z=8 (full circles), 13 (empty circles) and 16 (full squares) measured at θ_{Lab}=2.5° (ref. [2]). The histograms are the results of the two-body calculation. b) The value of the average ratio $< A/Z >$ as a function of the Z of the projectile fragments measured at θ_{Lab}=2.5° (ref. [2]). The full circles are the data whereas the empty circles are the results of the two-body calculations.The associated vertical bars are the standard deviations. The projectile A/Z value is indicated by the dotted line. c) Angle integrated isotopic distributions for Z=1 (full circles) and 2 (empty circles) particles emitted by the projectile (this experiment). The predictions of the two-body model including a multisequential binary-decay mechanism are shown as full and dashed histograms for Z=1 and 2 respectively.

Fig. 11 Bidimensional plots showing the theoretical fragment-fragment charge correlation in the forward wall: a) two-body multisequential model b) three-body multisequential model (see text). The contour plots are linear according to the scale given on the right. The line corresponding to $Z_1 + Z_2$=18 is shown.

Fig. 12 The angle-integrated coincidence cross-sections for several projectile fragments are given as a function of the coincident fragment charge (element symbols and scales, as indicated). The results for the cross-section integrated over all the projectile fragments is also reported (full points, see also Fig.3). The predictions of the two-body model including a multisequential binary-decay mechanism, (see text), are shown with dashed (for single coincident projectile fragment) and solid (all coincident projectile fragments) lines.

Fig. 13 The average excitation energy per nucleon of the primary PLFs as determined in ref. [1] (full circles) as a function of the Z of the detected PLFs is compared to the predictions of the two-body (upper dashed line) and
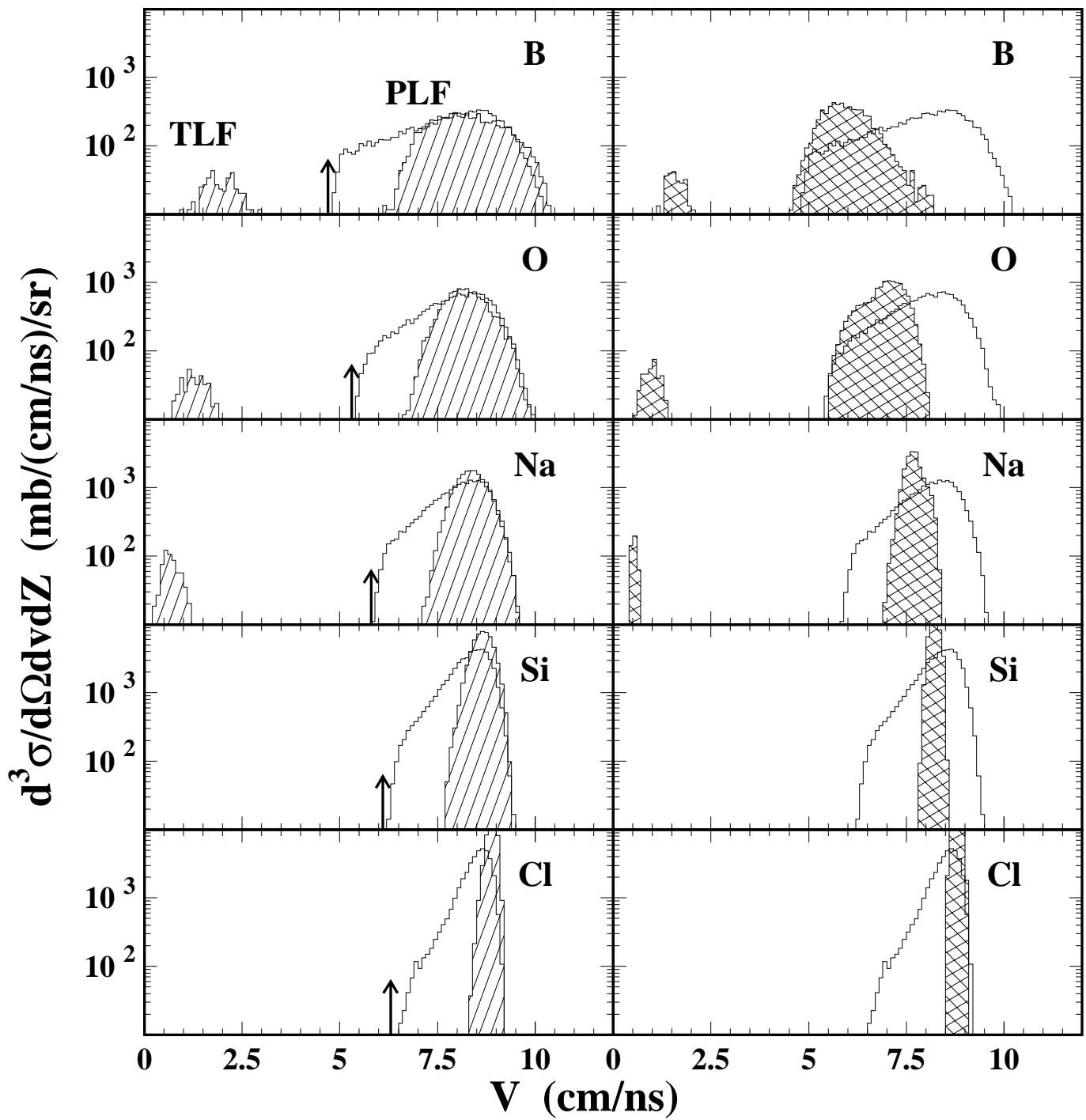
three-body (lower dashed line) calculations. The full squares are obtained by applying the calorimetric method of ref. [1] to the two-body simulations events to determine the excitation energy of the primary PLFs (see text for details). The vertical bars and the hatched and gray area represent the standard deviations of the distributions.

PL

Z=18

a)

Fast component (a.u.)

Slow component (a.u.)

10^3

Z=8

α

t

d

10^2

p

b)

Time of Flight (a.u.)

a)

b)

M_{TOT}, M_{CP}

YIELD

$\langle T \rangle$ (MeV)

a)

Z=8

Z=13

Z=16

$d^3\sigma/d\Omega dAdZ$ (mb/sr)

A (amu)

b)

$\langle A/Z \rangle$

A/Z = 2.22

Z

c)

$d^2\sigma/dAdZ$ (mb)

A (amu)